
Compressing Vision Transformers in Geospatial Transfer Learning with Manifold-Constrained Optimization

Thomas Snyder

Yale University

201 York Street, New Haven, CT 06511, USA
 thomas.snyder@yale.edu

H. Lexie Yang

Geospatial Science and Human Security Division
 Oak Ridge National Laboratory
 Oak Ridge, TN 37831 USA
 yangh@ornl.gov

Stefan Schnake

Computer Science and Mathematics Division
 Oak Ridge National Laboratory
 Oak Ridge, TN 37831 USA
 schnakesr@ornl.gov

Steffen Schotthöfer

Computer Science and Mathematics Division
 Oak Ridge National Laboratory
 Oak Ridge, TN 37831 USA
 schotthofers@ornl.gov

Abstract

Deploying geospatial foundation models on resource-constrained edge devices demands compact architectures that maintain high downstream performance. However, their large parameter counts and the accuracy loss often induced by compression limit practical adoption. In this work, we leverage manifold-constrained optimization framework DLRT to compress large vision transformer-based geospatial foundation models during transfer learning. By enforcing structured low-dimensional parameterizations aligned with downstream objectives, this approach achieves strong compression while preserving task-specific accuracy. We show that the method outperforms of-the-shelf low-rank methods as LoRA. Experiments on diverse geospatial benchmarks confirm substantial parameter reduction with minimal accuracy loss, enabling high-performing, on-device geospatial models.

1 Introduction

The proliferation of high-resolution remote-sensing imagery and advances in large-scale training have driven rapid progress in geospatial representation learning for applications as mapping of built environments [1], disaster management [10], and gravity anomaly mapping [20]. Recent work [4] shows clear benefits from building large foundation models (FMs) and scaling vision-transformer (ViT) architectures to hundreds of millions or billions of parameters for remote sensing tasks, yielding strong generalization across multiple downstream tasks, including classification, segmentation and object detection. In practice, geospatial applications often begin with large FMs, which can then be fine-tuned through transfer learning to support specific use cases such as land-cover mapping, disaster response, and near-real-time monitoring. In operational and deployment environment, practitioners require models that (i) meet limited memory and latency constraints, and (ii) preserve task-specific

accuracy and calibration. While these models enable strong transfer performance, their large size and computational demands high operational costs, making serving such large FM based models impractical for many practitioners for edge or local deployment, where limited compute and memory resources are available [14]. Model compression methods often invoke an often ambiguous trade-off between parameter reduction and reliable downstream performance.

Recently, principled methods to impose a structured low-rank parameterization during training for model compression have been proposed. Dynamical low-rank training (DLRT) approaches [16, 14, 13] restrict weight updates to a low-dimensional manifold; this yields both practical memory savings and provable approximation/descent guarantees under standard assumptions.

In this paper we present a careful, large-scale empirical study that applies manifold-constrained DLRT methods to compress ViT-based geospatial foundation models *during* supervised transfer learning. Our study targets both ImageNet21k-initialized ViTs [6] and the medium-resolution (MR) version of OReole geospatial FMs [5], and focuses on land-cover classification tasks on standard benchmarks.

2 Recap: Dynamical Low-Rank Training

We consider a neural network f as a concatenation of L layers $z^{\ell+1} = \sigma^\ell(W^\ell z^\ell)$ with matrix valued¹ parameters $W^\ell \in \mathbb{R}^{n \times n}$, layer input $z^\ell \in \mathbb{R}^{n \times b}$ and element-wise nonlinear activation σ^ℓ . The data X constitutes the input to the first layer, i.e. $z^0 = X$. The network is trained on a loss function \mathcal{L} which we assume to be locally bounded with a Lipschitz continuous gradient. Throughout this work, we call a network in the standard format a "baseline" network.

Low-rank Compression: The compression of the network for training and inference is typically facilitated by approximating the layer weight matrices by a low-rank factorization $W^\ell = U^\ell S^\ell V^{\ell, \top}$ with $U^\ell, V^\ell \in \mathbb{R}^{n \times r}$ and $S^\ell \in \mathbb{R}^{r \times r}$, where r is the rank of the factorization. For simplicity of exposition we drop the layer index ℓ and consider a single layer in the following. We denote the gradient flow of the layer by $\dot{W}(t) = -\nabla_W \mathcal{L}(W(t))$.

Manifold constrained low-rank training If $\text{rank}(S) = r$, the factorization USV^\top is element of the manifold of rank r matrices \mathcal{M}_r . Recent work [16] interprets the low-rank training process as the evolution the gradient flow projected onto \mathcal{M}_r , i.e., $\dot{W}_r(t) = -P_{\mathcal{M}_r} \nabla_W \mathcal{L}(W(t))$. This point of view is useful to build efficient optimizers for low-rank layers for model compression with improved convergence behavior [22, 9, 7], resource constrained federated learning [14], low-rank finetuning [15] and it has been extended to momentum-based optimizers [17].

Below we summarize the method, called *dynamical low-rank training* (DLRT).

Basis Augmentation: The method first augments the current bases U^t, V^t at optimization step t by their gradient dynamics $\nabla_U \mathcal{L}, \nabla_V \mathcal{L}$ via

$$\hat{U} = \text{orth}([U^t \mid \nabla_U \mathcal{L}(U^t S^t V^{t, \top})]), \quad \hat{V} = \text{orth}([V^t \mid \nabla_V \mathcal{L}(U^t S^t V^{t, \top})]) \in \mathbb{R}^{n \times 2r},$$

to double the rank of the low-rank representation and subsequently creates orthonormal bases \hat{U}, \hat{V} . The span of \hat{U} contains U^t , which is needed to ensure that the loss does not increase during augmentation, and a first-order approximation of $\text{span}(U^{t+1})$ using the exact gradient flow for U , see [14, Theorem 2] for details. Geometrically, the latent space

$$\mathcal{S} = \{\hat{U} Z \hat{V}^\top : Z \in \mathbb{R}^{2r \times 2r}\} \tag{1}$$

can be seen as subspace

of the tangent plane of \mathcal{M}_r at $U^t S^t V^{t, \top}$, see Figure 1.

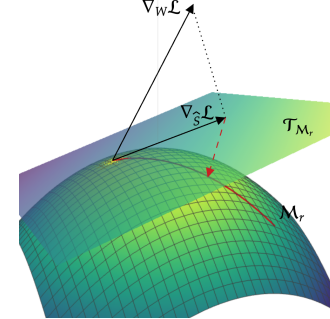


Figure 1: Geometric interpretation of DLRT. First, we compute the parametrization of the tangent plane $\mathcal{T}_{\mathcal{M}_r}$. Then we compute the projected gradient update with $\nabla_{\hat{S}} \mathcal{L}$. Lastly, we retract the updated coefficients back onto the manifold \mathcal{M}_r . The regularizer \mathcal{R} effectively changes the local curvature of \mathcal{M}_r .

¹Extensions to tensor-valued layers, e.g. in CNNs, are available [22]

Latent Space Training: We update the latent coefficients \widehat{S} via a Galerkin projection of the training dynamics onto the latent space \mathcal{S} . The latent coefficients \widehat{S} are updated by integrating the projected gradient flow $\dot{\widehat{S}} = -\widehat{U}^\top \nabla_W \widehat{\mathcal{L}} \widehat{V} = -\nabla_{\widehat{S}} \widehat{\mathcal{L}}$ using stochastic gradient descent or an other suitable optimizer for a number of s_* local iterations, i.e.

$$\widehat{S}_{s+1} = \widehat{S}_s - \lambda \nabla_{\widehat{S}} \mathcal{L} \quad s = 0, \dots, s_* - 1. \quad (2)$$

Equation (2) is initialized with $\widehat{S}_0 = \widehat{U}^\top U^t S^t V^{t,\top} \widehat{V} \in \mathbb{R}^{2r \times 2r}$, and we set $\tilde{S} = \widehat{S}_{s_*}$

Truncation: Finally, the latent solution $\widehat{U} \tilde{S} \widehat{V}^\top$ is retracted back onto the manifold \mathcal{M}_r . The retraction can be computed efficiently by using a truncated SVD of \tilde{S} that discards the smallest r singular values. To enable rank adaptivity, the new rank r_1 instead of r can be chosen by a variety of criteria, e.g., a singular value threshold $\|[\zeta_{r_1}, \dots, \zeta_{2r}]\|_2 < \vartheta$. Once a suitable rank is determined, the bases U and V are updated by discarding the basis vectors corresponding to the truncated singular values.

Computational cost: The computational cost of DLRT is asymptotically the same as LoRA [8], since the reconstruction of the full weight matrix W is never required. The orthonormalization accounts for $\mathcal{O}(nr^2)$, the regularizer \mathcal{R} for $\mathcal{O}(r^3)$, and the SVD for $\mathcal{O}(r^3)$ floating point operations. When using multiple coefficient update steps $s_* > 1$, the amortized cost is indeed lower than that of LoRA, since only the gradient with respect to \widehat{S} is required in most updates.

Convergence: Careful construction of the tangent space during the augmentation step guarantees loss descent of the DLRT scheme [15], i.e.,

$$\mathbb{E}_{\xi_{t+1}}[L(W_r^{t+1})] \leq L(W_r^t) - \lambda \left(1 - \frac{L\lambda^2}{2}\right) \mathbb{E}_{\xi_1}[\|P_{\mathcal{M}_r} \nabla_{W_r} \mathcal{L}(W_r^t, \xi_t)\|^2] + L \mathbb{E}_{\xi_1}[\|W_r^{t+1} - \widehat{U} \tilde{S} \widehat{V}^\top\|],$$

where L is the Lipschitz constant and ξ_t denotes the stochastic influence of batch descent. This is effectively the projected loss descent of stochastic gradient descent, except for the retraction error term $L \mathbb{E}_{\xi_1}[\|W_r^{t+1} - \widehat{U} \tilde{S} \widehat{V}^\top\|]$. In practice, this term vanishes as a suitable manifold rank and basis is found [3], paving the way for convergence of the scheme [15, Theorem 2] under standard assumptions, i.e.,

$$\liminf_{T \rightarrow \infty} \mathbb{E}[\|P_{\mathcal{M}_r} \nabla_{W_r} \mathcal{L}(W_r^t, \xi_t)\|^2] = 0$$

Error control and robustness: Orthogonality of the bases and the manifold constraint optimization enables error control of the low-rank scheme in relation to full-rank training. That is, the solution of the original gradient flow $W(t)$ and the projected (Riemannian) gradient flow $W_r(t)$ are close to each other, if they start from the same initial condition [15, Theorem 3],

$$\|W(t) - W_r^t\| \leq c_1 \varepsilon + c_2 \lambda + \frac{c_3 \vartheta}{\lambda},$$

where $c_{1,2,3} > 0$ do not depend on time or the geometry of the manifold.

Lastly, the method is compatible with regularization schemes [18] acting on the low-rank latent space of the manifold representation to improve adversarial robustness, an important property for geospatial applications.

3 Low-Rank Compressed Transfer Learning for Geospatial Vision Transformers

Test case setup We explore the capabilities of low-rank manifold training and concurrent automatic compression of geospatial foundation models. We target the image classification problem as the downstream task using three well-known remote sensing benchmark datasets, NWPU[2], AID[19], and UCM[21]. The test cases have small train-to-validation set ratios of 50% for UCM, 20% for AID, and 10% for NWPU, rendering them challenging benchmarks for transfer learning. Test case and data preprocessing details are provided in Section A.

Table 1: Validation accuracy comparison (in percent) of foundation models pretrained on ImageNet-21k with supervised pretraining, and Oreole style [4] MAE self supervised pretraining. The models are compressed during transfer learning on the UCM, AID, and NWPU downstream datasets. "c.r." denotes compression ratio, i.e. the percentage of removed parameters compared to baseline. Each cell denotes the mean and standard deviation over 10 runs with stochastic gradient descent.

Model	UCM				AID				NWPU							
	Baseline	DLRT	c.r.	LoRA	c.r.	Baseline	DLRT	c.r.	LoRA	c.r.	Baseline	DLRT	c.r.	LoRA	c.r.	
ImageNet21k	ViT-B16	98.13 \pm 0.15	97.67 \pm 0.13	68.63	95.37 \pm 0.34	62.38	95.42 \pm 0.68	93.92 \pm 0.55	66.15	93.35 \pm 0.45	66.13	91.45 \pm 0.43	89.41 \pm 0.21	65.35	88.01 \pm 1.00	62.40
	ViT-H14	97.57 \pm 0.89	97.32 \pm 0.42	81.47	96.86 \pm 0.63	78.33	93.75 \pm 0.39	93.83 \pm 0.18	78.22	90.67 \pm 0.08	78.01	90.04 \pm 0.73	89.69 \pm 0.57	79.52	88.51 \pm 0.63	79.53
	ViT-G14	98.30 \pm 0.75	98.29 \pm 0.17	77.33	94.00 \pm 0.91	81.96	95.76 \pm 0.23	93.85 \pm 0.67	81.69	89.48 \pm 0.64	76.35	92.27 \pm 0.20	88.25 \pm 0.35	80.56	82.24 \pm 4.23	79.65
OReole-MR	ViT-B16	97.87 \pm 0.94	96.74 \pm 0.18	64.32	95.05 \pm 0.89	62.42	95.01 \pm 0.43	90.12 \pm 0.83	70.13	88.02 \pm 0.98	62.35	91.35 \pm 1.10	84.22 \pm 0.20	63.78	81.06 \pm 0.77	63.41
	ViT-H14	98.56 \pm 0.63	97.17 \pm 0.67	80.83	94.28 \pm 0.78	77.69	96.04 \pm 0.28	92.91 \pm 0.56	78.22	90.75 \pm 0.75	78.03	92.79 \pm 0.24	88.80 \pm 0.80	78.22	88.01 \pm 0.21	76.65
	ViT-G14	98.30 \pm 0.75	98.29 \pm 0.17	77.33	94.00 \pm 0.91	81.96	95.76 \pm 0.23	93.85 \pm 0.67	81.69	89.48 \pm 0.64	76.35	92.27 \pm 0.20	88.25 \pm 0.35	80.56	82.24 \pm 4.23	79.65

Foundation models. We consider both "classic" ViT models [6] and the OReole-MR family of geospatial foundation models (FMs) [5]. The classic ViTs include ViT-B16 and ViT-H14, using HuggingFace checkpoints [google/vit-base-patch32-224-in21k](https://huggingface.co/google/vit-base-patch32-224-in21k) and [google/vit-huge-patch14-224-in21k](https://huggingface.co/google/vit-huge-patch14-224-in21k), pretrained on ImageNet-21k [12]. Architectural details are provided in Table 2.

The OReole-MR models follow the ViT architecture but adopt a self-supervised pretraining scheme, embedding the ViT backbone within a masked autoencoder (MAE) pipeline [4]. Pretraining is conducted on the unlabeled Million-AID dataset [11]. For downstream tasks in this work, we extract the pretrained ViT backbone from the MAE and attach a task-specific classification head.

For a pretrained foundation model, we apply a truncated SVD of rank r to each fully connected layer, obtaining U, S, V factors that initialize low-rank training consistent with the pretrained weights. The classification head is excluded, as its rank equals the number of classes.

Transfer learning: We compare the compressed transfer learning capabilities of DLRT against two baselines: uncompressed transfer learning with full models, and training only the low-rank factors, akin to the popular LoRA method [8]. For each combination of training method, downstream dataset, and model, hyperparameters were chosen via an initial sweep (see Table 4). We find that the learning rate most strongly affects validation accuracy, with smaller values performing best, which consistent with transfer learning. In contrast, the DLRT hyperparameters τ and s_* show an order of magnitude weaker correlation, indicating robustness to their choice.

For both LoRA and DLRT applied to the OReole-MR models, we found it beneficial to include a single warm-up epoch of standard (uncompressed) transfer learning before applying low-rank adaptation. This simple step improved final validation accuracy by up to 10% compared to training without warm-up, a trend observed consistently across both DLRT and LoRA-based training. Interestingly, this effect was absent for ImageNet-pretrained checkpoints, which we attribute to the difference in pretraining schemes: the self-supervised pretraining of OReole-MR appears less aligned with the low-rank subspace, whereas the supervised pretraining of ImageNet models yields weights more naturally compatible with DLRT- or LoRA-style compression. A more detailed investigation of this phenomenon is left to future work.

Results: Table 1 compares validation accuracy on UCM, AID, and NWPU for ViT models pretrained on ImageNet-21k with either supervised or Oreole-MR MAE pretraining. We evaluate baseline finetuning against DLRT and LoRA under comparable compression ratios. Results are reported as the mean and standard deviation over 10 runs.

DLRT consistently preserves accuracy within 0.5–1% of the baseline in the UCM dataset, while removing 64–82% of parameters, whereas LoRA exhibits larger drops in validation accuracy, especially for the OReole-MR models. In the more challenging AID and NWPU test cases with smaller train-to-test data ratio, the accuracy of low-rank method drops more compared to the baseline, however DLRT surpasses LoRA based training by 1–6% validation accuracy. Across pretraining types and model scales, DLRT outperforms LoRA in accuracy retention under equal compression. Finally, we observe that OReole-MR based FMs achieve the highest validation accuracies across test cases, but are harder to compress in low-rank format, compared to the ImageNet-based models.

4 Conclusion

This study demonstrates that manifold-constrained low-rank optimization can substantially compress vision transformer-based geospatial foundation models while preserving performance of downstream tasks. By enforcing structured parameterizations aligned with transfer learning objectives, the approach consistently outperforms standard low-rank baselines such as LoRA across multiple datasets and pretraining schemes. These findings highlight the practicality of deploying compact, high-performing geospatial models on constrained hardware, paving the way for broader real-world applications. Future work may improve alignment with self-supervised pretraining, and extensions to additional geospatial tasks.

References

- [1] J. Arndt and D. Lunga. Large-scale classification of urban structural units from remote sensing imagery. *IEEE Journal of Selected Topics in Applied Earth Observations and Remote Sensing*, 14:2634–2648, 2021.
- [2] G. Cheng, J. Han, and X. Lu. Remote sensing image scene classification: Benchmark and state of the art. *Proceedings of the IEEE*, 105(10):1865–1883, 2017.
- [3] D. Coquelin, K. Flügel, M. Weiel, N. Kiefer, C. Debus, A. Streit, and M. Götz. *Harnessing Orthogonality to Train Low-Rank Neural Networks*. IOS Press, Oct. 2024.
- [4] P. Dias, A. Tsaris, J. Bowman, A. Potnis, J. Arndt, H. L. Yang, and D. Lunga. OReole-FM: successes and challenges toward billion-parameter foundation models for high-resolution satellite imagery. arXiv preprint arXiv:2410.19965, 2024. ACM SIGSPATIAL short paper; extended arXiv version.
- [5] P. Dias, A. Tsaris, J. Bowman, A. Potnis, J. Arndt, H. L. Yang, and D. Lunga. Oreole-fm: successes and challenges toward billion-parameter foundation models for high-resolution satellite imagery. In *Proceedings of the 32nd ACM International Conference on Advances in Geographic Information Systems, SIGSPATIAL ’24*, page 597–600. ACM, Oct. 2024.
- [6] A. Dosovitskiy, L. Beyer, A. Kolesnikov, D. Weissenborn, X. Zhai, T. Unterthiner, M. Dehghani, M. Minderer, G. Heigold, S. Gelly, J. Uszkoreit, and N. Houlsby. An image is worth 16x16 words: Transformers for image recognition at scale, 2021.
- [7] A. Hnatiuk, J. Kusch, L. Kusch, N. R. Gauger, and A. Walther. Stochastic aspects of dynamical low-rank approximation in the context of machine learning. *Optimization Online*, 2024.
- [8] E. J. Hu, Y. Shen, P. Wallis, Z. Allen-Zhu, Y. Li, S. Wang, L. Wang, and W. Chen. Lora: Low-rank adaptation of large language models. *arXiv preprint arXiv:2106.09685*, 2021.
- [9] J. Kusch, S. Schotthöfer, and A. Walter. An augmented backward-corrected projector splitting integrator for dynamical low-rank training. *arXiv preprint arXiv:2502.03006*, 2025.
- [10] M. Laverdiere, L. Yang, M. Tuttle, and C. Vaughan. Rapid structure detection in support of disaster response : A case study of the 2018 kilauea volcano eruption. Oak Ridge National Laboratory (ORNL), Oak Ridge, TN (United States), 09 2020.
- [11] Y. Long, G.-S. Xia, S. Li, W. Yang, M. Y. Yang, X. X. Zhu, L. Zhang, and D. Li. On creating benchmark dataset for aerial image interpretation: Reviews, guidances and million-aid, 2021.
- [12] T. Ridnik, E. Ben-Baruch, A. Noy, and L. Zelnik-Manor. Imagenet-21k pretraining for the masses, 2021.
- [13] S. Schotthöfer, T. Klein, and J. Kusch. A geometric framework for momentum-based optimizers for low-rank training. arXiv preprint arXiv:2506.17475, 2025. Momentum-aware extension of DLRT; geometric optimizer for low-rank training.
- [14] S. Schotthöfer and M. P. Laiu. Federated dynamical low-rank training with global loss convergence guarantees. *arXiv preprint arXiv:2406.17887*, 2024.

- [15] S. Schotthöfer, E. Zangrando, G. Ceruti, F. Tudisco, and J. Kusch. GeoLoRA: Geometric integration for parameter efficient fine-tuning. arXiv preprint arXiv:2410.18720, 2024. Geometric integration and theoretical guarantees for low-rank adapters (descent and convergence).
- [16] S. Schotthöfer, E. Zangrando, J. Kusch, G. Ceruti, and F. Tudisco. Low-rank lottery tickets: finding efficient low-rank neural networks via matrix differential equations. arXiv preprint arXiv:2205.13571, 2022. NeurIPS 2022; dynamical low-rank perspective and error/descent guarantees.
- [17] S. Schotthöfer, T. Klein, and J. Kusch. A geometric framework for momentum-based optimizers for low-rank training, 2025.
- [18] S. Schotthöfer, H. L. Yang, and S. Schnake. Dynamical low-rank compression of neural networks with robustness under adversarial attacks, 2025.
- [19] G.-S. Xia, J. Hu, F. Hu, B. Shi, X. Bai, Y. Zhong, L. Zhang, and X. Lu. Aid: A benchmark data set for performance evaluation of aerial scene classification. *IEEE Transactions on Geoscience and Remote Sensing*, 55(7):3965–3981, July 2017.
- [20] L. Yang, D. Lunga, D. King, J. Arndt, J. Bowman, and R. Stewart. Exploring Spatially Distributed Deep Learning Models for Global Gravitational Mapping. In *AGU Fall Meeting Abstracts*, volume 2021, pages EP12C–05, Dec. 2021.
- [21] Y. Yang and S. Newsam. Bag-of-visual-words and spatial extensions for land-use classification. In *Proceedings of the 18th SIGSPATIAL International Conference on Advances in Geographic Information Systems*, GIS ’10, page 270–279, New York, NY, USA, 2010. Association for Computing Machinery.
- [22] E. Zangrando, S. Schotthöfer, G. Ceruti, J. Kusch, and F. Tudisco. Geometry-aware training of factorized layers in tensor tucker format. In A. Globerson, L. Mackey, D. Belgrave, A. Fan, U. Paquet, J. Tomczak, and C. Zhang, editors, *Advances in Neural Information Processing Systems*, volume 37, pages 129743–129773. Curran Associates, Inc., 2024.
- [23] E. Zangrando, S. Schotthöfer, G. Ceruti, J. Kusch, and F. Tudisco. Geometry-aware training of factorized layers in tensor tucker format, 2024.

Table 2: Architecture details of the used ViT backbones. The table reports the patch size, number of transformer layers, hidden embedding size, and total parameter count (in millions) for each model variant. The parameter count for ViT-G14 is only for OReole given that there is no ViT-G14 for ImageNet, denoted by an asterisk.

Model	Patch Size	Layers	Hidden Size	Total Parameters [Millions]
ViT-B16	16	12	768	64.33
ViT-H14	14	32	1280	472.67
ViT-G14	14	32	1536	680.45*

Table 3: Constant hyperparameters used across all sweep experiments. These values remained fixed for every model, dataset, and training configuration to ensure consistency and comparability of results. The listed parameters include both general training settings and method-specific configurations for DLRT

Hyperparameter	Value
training batch size	16
validation batch size	256
training epochs	10
initial rank (for truncated SVD)	100
maximum rank for DLRT augmentation	200
coefficient finetuning epochs (DLRT, LoRA)	2

A Test case descriptions

A.0.1 UCM

The University of California, Merced (UCM) Land Use Dataset is a benchmark dataset in remote sensing and computer vision, introduced in [21]. It covers urban areas across the United States. It comprises 2,100 high-resolution aerial RGB images, each measuring 256×256 pixels, categorized into 21 land use classes with 100 images per class. The images were manually extracted from the USGS National Map Urban Area Imagery collection, covering various urban areas across the United States. The dataset contains images with spatial resolution approximately 0.3 meters per pixel (equivalent to 1 foot), providing detailed visual information suitable for fine-grained scene classification tasks.

A.0.2 AID

The Aerial Image Dataset (AID) [19] includes 10,000 images from Google Earth, 600×600px, with varying resolutions (0.5–8 meters/px), spread across 30 classes with slight imbalance in distribution.

A.0.3 NWPU

Remote Sensing Image Scene Classification[2], created by Northwestern Polytechnical University (NWPU-RESISC45) is an aerial imaging dataset that has 31,500 images, 256×256px, from global regions via Google Earth, covering 45 balanced categories with resolutions from 0.2 to 30 meters/px.

A.1 Data preprocessing

We normalize the training and validation data with mean [0.485, 0.456, 0.406] and standard deviation [0.229, 0.224, 0.225] for the rgb image channels. Images are resized to 244x244 pixels for the vision transformers during the training pipeline, no matter their initial size.

B Model Details

We refer to [6] for the full description of the vision transformer architecture and display the architecture differentiators for the models used in this work in Table 2.

Table 4: Hyperparameter sweep results by dataset, method, and model. γ = weight decay, λ = learning rate, s_* = number of local iterations for the S update on the tangent space. The threshold is defined as $\tau = \vartheta \cdot \|\zeta_{r_1}, \dots, \zeta_{2r}\|_2$.

Model	UCM				AID				NWPU			
	γ	λ	s_*	τ	γ	λ	s_*	τ	γ	λ	s_*	τ
ImageNet1k	ViT-B16 Baseline	0.00062	9.64e-5	—	—	0.04055	8.66e-5	—	—	0.04120	5.58e-5	—
	ViT-B16 Low-Rank	0.02461	1.33e-4	181	0.0176	0.03092	2.59e-4	236	0.0789	0.02692	9.13e-5	36
	ViT-H14 Baseline	0.01437	2.49e-4	—	—	0.02637	3.49e-4	—	—	0.03377	2.71e-4	—
	ViT-H14 Low-Rank	0.00283	5.85e-4	232	0.0497	0.04137	2.88e-4	89	0.0081	0.00554	4.79e-4	57
OReole-MR	ViT-B16 Baseline	0.03720	1.09e-4	—	—	0.00201	8.55e-5	—	—	0.01662	6.69e-5	—
	ViT-B16 Low-Rank	0.03724	1.66e-4	22	0.0379	0.03156	1.81e-4	64	0.0073	0.02205	1.98e-4	226
	ViT-H14 Baseline	0.02246	7.40e-5	—	—	0.02222	7.37e-5	—	—	0.00146	8.96e-5	—
	ViT-H14 Low-Rank	0.03318	2.01e-4	119	0.0085	0.01318	1.94e-4	221	0.0393	0.03547	3.16e-4	248
	ViT-G14 Baseline	0.01121	6.97e-5	—	—	0.01813	6.32e-5	—	—	0.04006	8.38e-5	—
	ViT-G14 Low-Rank	0.04661	2.35e-4	24	0.0235	0.02901	9.03e-5	160	0.0295	0.04897	1.28e-4	113

Table 5: Correlation of tolerance, local iteration, learning rate, and weight decay with validation accuracy for the hyperparameter sweep. Negative correlations for learning rate across all models confirm that smaller values are preferred for stable training.

Model	τ	s_*	λ	γ
ImageNet21k	ViT-B16 (Full Rank)	-	-	-0.864 -0.042
	ViT-H14 (Full Rank)	-	-	-0.818 -0.052
	ViT-B16 (Low Rank)	-0.123	-0.024	-0.932 0.034
	ViT-H14 (Low Rank)	-0.023	0.03	-0.895 0.025
OReole-MR	ViT-B16 (Full Rank)	-	-	-0.83 0.038
	ViT-H14 (Full Rank)	-	-	-0.885 0.094
	ViT-B16 (WLR)	0.081	0.026	-0.807 0.042
	ViT-H14 (WLR)	-0.012	0.009	-0.876 -0.096

C Training Details

We display the hyperparameters, that remain constant across all runs in Table 3. The lower part of the table denotes DLRT hyperparameters. We remark that in the last two epochs of training, we freeze the low-rank bases U, V and only train S . This ensures that in the final steps of DLRT or LoRA, a sudden basis change does not affect validation performance. This trick is consistent with the loss, convergence and error bound analysis of DLRT [23]. In practice, one does not expect much changes in the low-rank basis after a certain number of augmentation-truncation steps [3].

The results of the hyperparameter sweeps can be found in Table 4. We perform a random sweep of at least 200 runs per model/data/method combination, where we vary the choice of weight-decay, learning rate, as well as local iterations and relative truncation tolerance $\vartheta = \tau \|W_r\|_F$. We chose the same hyperparameters for LoRA and DLRT.

D Hardware

All trainings and sweeps were run on single workstation GPUs, using NVIDIA RTX A6000 40GB and NVIDIA RTX 4090 24GB GPUS.